C. R. Physique 13 (2012) 246–256

Contents lists available at SciVerse ScienceDirect

Comptes Rendus Physique

www.sciencedirect.com

Use of large scale facilities for research in metallurgy

Precipitate characterisation in metallic systems by small-angle X-ray or neutron scattering

Caractérisation des précipités dans les systèmes métalliques utilisant la diffusion aux petits angles des rayons X ou des neutrons

Frédéric De Geuser *, Alexis Deschamps

SIMaP, Grenoble INP – CNRS – UJF, BP. 75, 38402 Saint Martin d'Hères cedex, France

ARTICLE INFO

Article history:
Available online 27 January 2012

Keywords:
Small-angle scattering
SAXS
SANS
Precipitation

Mots-clés :
Diffusion aux petits angles
DXPA
DNPA
Précipitation

ABSTRACT

Small-angle scattering enables the extraction of precise, quantitative information about nano-scale precipitate microstructures. It can be used with X-rays (SAXS) or neutrons (SANS). This paper presents simple methods for extracting information on the precipitate size and volume fraction from SAS spectra. The various possibilities for obtaining precipitate size are reviewed, and the meaning of their differences is discussed. Examples of applications for complex precipitate microstructure measurements are given in the following areas: kinetic in-situ measurements in Fe–Cu and Fe–Nb–C alloys, non-stoichiometric precipitation in an Al–Zn–Mg–Cu alloy studied by anomalous SAXS (ASAXS), and precipitation mapping in weld cross-sections.

RÉSUMÉ

La technique de diffusion aux petits angles permet l'obtention d'informations précises et quantitatives sur les microstructures de précipitation à l'échelle nanométrique. Elle peut être utilisée avec des rayons X (DXPA ou SAXS) ou avec des neutrons (DNPA ou SANS). Cet article présente des méthodes simples pour extraire des informations sur les tailles et fractions volumiques des précipités à partir des spectres de diffusion. Différentes méthodes sont indiquées, ainsi que leur signification et différences. Des exemples d'applications sont donnés pour la caractérisation de microstructures complexes dans les cas suivants : mesures in-situ de cinétiques de précipitation dans Fe–Cu et Fe–Nb–C, précipitation non stoechiométrique évaluée par diffusion anormale des rayons X (ASAXS), et cartographie de précipitation dans les sections transverses de soudures.

1. Introduction

Among all phase transformations in metallic alloys, fine-scale precipitation (meaning at a scale between 1 and 50 nm) is one of the most effective to obtain high strength materials. Controlling and optimising the strength, as well as other properties impacted by precipitation (e.g. ductility, toughness, corrosion resistance, ...), is, of course, possible only if an

* Corresponding author.
E-mail addresses: frederic.de-geuser@simap.grenoble-inp.fr (F. De Geuser), alexis.deschamps@simap.grenoble-inp.fr (A. Deschamps).

1631-0705/$ – see front matter
doi:10.1016/j.crhy.2011.12.008

in-depth, quantitative understanding of the precipitation microstructure is obtained. It is also of importance to obtain as precise information as possible about the path leading to the final desired microstructure, and thus to characterise the kinetics of the phase transformation process (e.g. [1]). The information sought about precipitates is structural (phase, stable or metastable), chemical (composition, which is often out-of equilibrium), morphological (shape, habit plane, etc.), and about distribution (size and size distribution, volume fraction). No experimental technique can provide all these information at once, and it is usually necessary to combine local techniques (like transmission electron microscopy or atom probe tomography) with more global techniques that provide average information on a large population of precipitates. In this article we will focus on Small-Angle Scattering (SAS) techniques, which have been developed since more than 50 years as a tool to quantify precipitate microstructures. A number of comprehensive reviews and books exist that present in detail the theory and applications of this technique [2–6]. The purpose of this article is to present in a simple way how the characteristics of a precipitate microstructure can be extracted from SAS spectra. In a second part, applications on complex precipitation phenomena will be presented. It will be shown that using state-of-the-art experimental apparatus, it becomes possible to characterise effectively precipitation kinetics in cases of low volume fractions, changing precipitate chemistry, and to map heterogeneous microstructures such as welds.

2. Introductory considerations on the use of X-ray and neutron sources

Small-Angle Scattering (SAS) is an experimental technique that allows measuring some characteristics of the fluctuations of the scattering factor in a sample. Depending on the incident beam used, the nature of the scattering factor changes, and therefore one can tune the type of fluctuations that can be probed by changing the source type. For the study of metals, SAS techniques can be carried out either with X-rays (SAXS) or with neutrons (SANS). In the first case, the diffusion factor is proportional to the electronic density, and therefore to the atomic number. As a consequence, SAXS will evaluate fluctuations of atomic number (and thus of composition) within the sample. Additionally, the scattering factor of a given element can be modified if the X-ray wavelength is chosen close to an absorption edge (K, L essentially). This enables some chemical selectivity of the measurements. Using a variable X-ray wavelength is called anomalous SAXS or ASAXS, and is very useful to assess the partitioning of a chemical element during phase separation [7].

Neutrons, on the other hand, are scattered by the atom nuclei and their magnetic moment. Thus using SANS it is possible to probe fluctuations in atomic scattering cross-section (which depend on the atomic species in a way not proportional to the atomic number) or in magnetic moment. The choice between X-rays and neutron scattering for a given measurement can be made according to the following guidelines:

- Advantage to X-rays (synchrotron source): for a system with a high contrast in atomic number, or when an absorption edge is available at a value of energy easily accessible for contrast enhancement. When fast measurements need to be done for in-situ measurements (measurements from 10 min down to less than 1 s). When one needs a small beam for mapping of heterogeneous microstructures. Note that when low counting times, anomalous measurements or high resolution are not needed, effective measurements can be made on laboratory sources (whether standard tubes or rotating anodes). SAXS works effectively for instance with most Al alloys (except the 6000 series due to low Z-contrast), but is generally more difficult with steels.
- Advantage to neutrons: for a system with low contrast in atomic number (or more specifically in electronic density), with high Z-number (neutrons traverse a much larger sample thickness), with low volume fraction (neutron wavelength can be chosen above the Bragg cut-off, which enables to suppress parasitic X-ray diffraction), with two phases of different magnetic properties. SANS is particularly useful for instance in steels, where volume fractions of precipitates are often very low, and where a strong magnetic contrast is usually present between precipitates and matrix.

It is interesting to notice that for precipitation in metallic systems, one of the advantages of X-rays over neutrons is the possibility of contrast variation by the choice of adequate energy close to absorption edges which are in available ranges for transition metals. In the area of organic solution studies, this advantage is completely reversed as no available absorption edge can be used for X-rays, whereas deuteration of the water can be used for contrast variation in SANS.

3. General equations and data interpretation

Small-angle scattering is governed by the general theory and equations of diffraction. An incident wave (only X-ray and neutrons are considered here) is scattered by individual objects (electrons for X-rays and nuclei for neutrons) contained in the sample. The scattered spherical waves are coherent and interfere. While considering the phase differences of the interfering waves at the scattering angle 2θ, it is convenient to introduce the scattering vector $\vec{q}$ (difference between the incident wave vector and the scattered wave vector), which amplitude is given by $q = \frac{4\pi}{\lambda}\sin(\theta)$. Each interfering wave issued by a scatterer positioned at $\vec{r}$ is then defined by a phase term $\exp(-i\vec{q}\vec{r})$ and an amplitude which is characteristic of the scatterer. The resulting wave for a given scattering angle 2θ (or a given scattering vector $\vec{q}$) is the sum of the contribution of all interfering waves. Small-angle scattering is only concerned by heterogeneities of a scale that is larger than the interatomic distances. It is then convenient to introduce $\rho(\vec{r})$, the number of scatterers per unit volume (multiplied

by their scattering factor, or scattering length for neutrons). $\rho(\vec{r})$ will be called scattering factor density. The scattered amplitude and the scattered intensity are then written:

$$A(\vec{q}) = \iiint_V \rho(\vec{r}) \exp(-\mathrm{i}\vec{q}\vec{r})\,\mathrm{d}V \tag{1}$$

$$I(\vec{q}) = \left|A(\vec{q})\right|^2 \tag{2}$$

A further practical simplification arises when considering an isotropically scattering sample. This can happen if the inhomogeneities are isotropic themselves (e.g. spherical precipitates) or if enough orientations of the objects are included in the beam (e.g. textureless polycrystal with small grain size compared with beamsize, or rotating objects in a liquid solution). In this case, the vectors can be replaced by their amplitude in the previous equations and:

$$I(q) = \left|\iiint_V \rho(r) \exp(-\mathrm{i}qr)\,\mathrm{d}V\right|^2 \tag{3}$$

Mathematically, this expression is the square modulus of the Fourier transform of the scattering factor density. The multiplication in the reciprocal space implied by this square modulus is equivalent to a convolution product in the direct space, so that *the scattered intensity is the Fourier transform of the autocorrelation* (*or Patterson*) *function of the scattering factor density*. Let $P(r)$ be this autocorrelation:

$$P(r) = \iiint_V \rho(r_1)\rho(r_2)\,\mathrm{d}V \quad \text{with } r = r_2 - r_1 = \text{constant} \tag{4}$$

By definition, $P(0) = V\overline{\rho^2}$ and in the absence of long range correlation, $P(\infty) = V\overline{\rho}^2$. This constant asymptotic value will give rise to no intensity except at $q = 0$, and only the deviation from this final value is of practical interest. Let

$$\gamma(r) = \frac{1}{V}\big(P(r) - P(\infty)\big) = \frac{P(r)}{V} - \overline{\rho}^2 \tag{5}$$

Here, $\gamma(r)$ is the autocorrelation of the fluctuation of electron (or scattering length) density, that is the autocorrelation of the excess electron (or scattering length) with respect to the average density. We can now rewrite the expression of the intensity using $\gamma(r)$, replacing $\mathrm{d}V$ by its value in spherical coordinates and replacing the phase term $\exp(-\mathrm{i}\vec{q}\vec{r})$ by its average in all orientations $\langle\exp(-\mathrm{i}\vec{q}\vec{r})\rangle = \frac{\sin(qr)}{qr}$ (Debye formula):

$$I(q) = V\int_V 4\pi r^2\gamma(r)\frac{\sin(qr)}{qr}\,\mathrm{d}r \tag{6}$$

Let us now consider a metallic alloy composed of precipitates of scattering factor density ρ_p embedded in a matrix of density ρ_m. For a single particle of simple shape, the intensity can be calculated through Eq. (6). For a spherical precipitate or radius R and of volume $V_p = 4/3\pi R^3$, it reads:

$$I_1(q, R) = (\rho_p - \rho_m)^2 V_p^2\left(3\frac{\sin(qR) - qR\cos(qR)}{(qR)^3}\right)^2 \tag{7}$$

For less simple precipitate shapes, the determination of the intensity scattered by a single particle may involve numerical integration over all orientations. If the precipitates in the system are not interfering (i.e. when the interparticle distance is large compared to the particle size), the total intensity is then the sum of the intensity scattered by each individual precipitate. If we consider a size dispersion function $f(R)$ corresponding to the density of precipitates of size R, the total intensity is the given by:

$$I(q) = \int_0^\infty f(R)I_1(q, R)\,\mathrm{d}R \tag{8}$$

The intensity scattered by a precipitate separated from the matrix by a sharp interface has an asymptotic behaviour described by the Porod law:

$$I \underset{q\to\infty}{\equiv} \frac{K_p}{q^4} \tag{9}$$

with K_p, the Porod constant, the signification of which will be discussed further in the paper. In practice, however, there is always a remaining background noise I_{Laue} which is essentially independent of q. It is mainly related to the Laue scattering

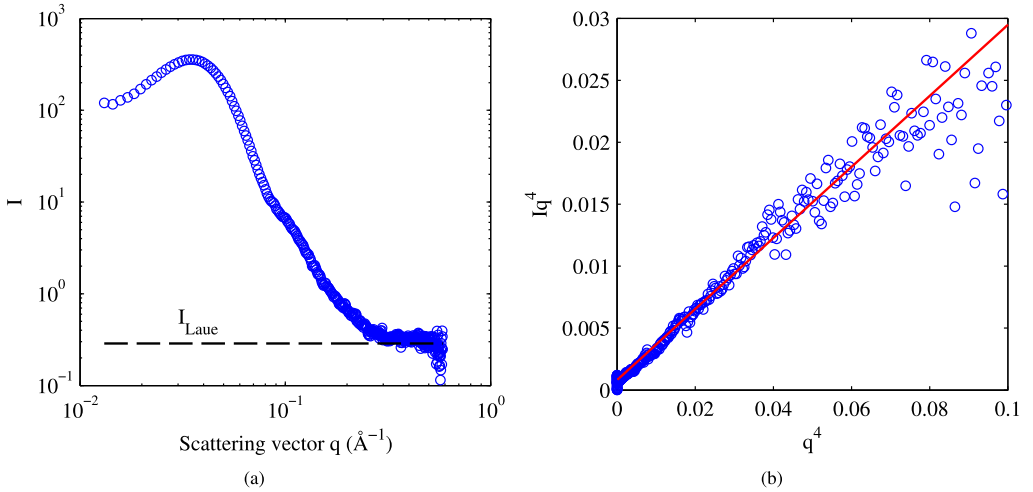

Fig. 1. Raw SAXS pattern of an Al–Li–Mg alloy: (a) Log–log plot showing the contribution of the Laue scattering; (b) $I_{\text{raw}}q^4$ vs. q^4 plot, the slope of which is equal to I_{Laue} (see text).

of the disordered solid solution, but also to possible fluorescence of secondary elements in the material or to inaccurate instrumental background correction. This leads to the following relation:

$$I_{\text{raw}} \underset{q\to\infty}{\equiv} \frac{K_p}{q^4} + I_{\text{Laue}} \tag{10}$$

This can be observed in Fig. 1(a) which represents the intensity scattered by an Al–Li–Mg alloy containing δ' Al_3Li precipitates. The constant background is evident in the figure. I_{Laue} can be easily determined by plotting $I_{\text{raw}}q^4$ vs. q^4 (cf. Fig. 1(b)):

$$I_{\text{raw}}q^4 \underset{q\to\infty}{\equiv} K_p + I_{\text{Laue}}q^4 \tag{11}$$

The slope of the linear part in Fig. 1(b) is equal I_{Laue} and can be subtracted from I_{raw} to obtain I. The result of this subtraction can be seen in Fig. 2(a). The high q range of the intensity follows a q^{-4} asymptote, justifying the use of Eq. (11) to correct for I_{Laue}.

It is now possible to use Eq. (8) to interpret the intensity of Fig. 2(a). The size dispersion function $f(R)$ is of particular importance in the case of precipitation in metallic system where the size dispersion is almost always large, so that the oscillations characteristic of monodisperse systems are seldom observed. In that case, different approaches are possible. The size distribution function can be determined by inversion methods such as indirect Fourier transforms [8,9] or maximum entropy methods [10]. Although time consuming, this techniques work very well. They will not be discussed in the present paper.

Another way is to use a model fitting approach using Eq. (8) with a known shape function and a model for the size dispersion. One such size dispersion model, very useful in practice, is the log-normal dispersion:

$$f(R) = \frac{1}{\sqrt{2\pi}\sigma R}\exp\left(-\frac{1}{2}\left(\frac{\ln(R_m/R)}{\sigma}\right)^2\right) \tag{12}$$

Although it is an ad hoc function, it has been shown to describe adequately the actual precipitate size distribution measured by transmission electron microscopy [11–13]. It can be described by two parameters, the median particle size R_m (which is close to the average size for moderately large size dispersion) and the parameter σ which is a measure of the width of the particle size distribution. It gives very good results on precipitation studies. The results of such model fitting is represented by the solid red line in Fig. 2(a). The parameter used for the fit are $R_m = 48.7$ Å and $\sigma = 0.20$. The fit is extremely good, except below the maximum of I. This originates from interference between particles. This is due to a very high volume fraction of precipitates in this Al–Li–Mg which leads to a lowering of the intensity at low q and an interference peak at a value related to $\frac{2\pi}{d}$, where d is the interparticle distance.

This kind of rough interpretation of the structure factor describing the interprecipitate interference is by no mean precise. For the purpose of demonstration, we have used a Percus–Yevick model with a hard-sphere potential [14], where the hard sphere represents an exclusion volume larger than the precipitate on which it is centred, in the local monodisperse approximation to fit the data of Fig. 2(a). The result of the fit is represented by the dashed green line ($R_m = 44.6$ Å and $\sigma = 0.24$). It reproduces the interference peak extremely well, but the fit is less good for larger value of q. This is likely to be due to the fact that the exclusion volume around a precipitate is probably not adequately described by an abrupt transition

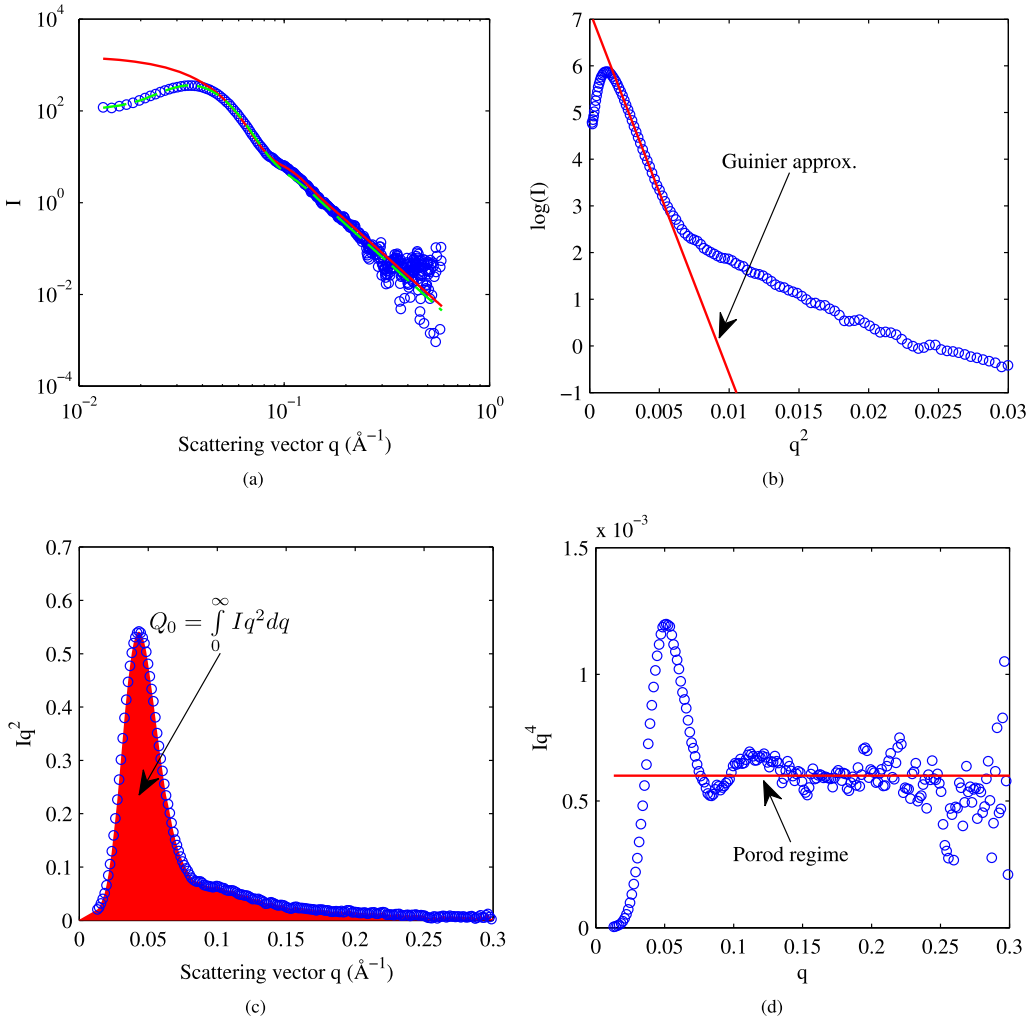

Fig. 2. SAXS intensity (same as Fig. 1), corrected from the Laue scattering: (a) Log–log plot with model fitting functions with interference (dashed line) and without interference (solid line); the solid line was obtained with $R_m = 48.7$ Å and $\sigma = 0.20$; (b) Guinier plot $\log(I)$ vs. q^2 with a linear fit giving $R_g = 48.3$ Å; (c) Kratky plot Iq^2 vs. q; the area (red) under the curve is the invariant Q and the maximum position yields to $R_g = 40$ Å (see text); (d) Porod plot Iq^4 vs. q showing damped oscillations around the Porod constant; the position of the first maximum gives a radius of 53.7 Å.

as in a hard sphere model. Comparison of the experimental data and the model fitting with and without interference shows that in real, size dispersed cases, a very good description of the intensity above the maximum can be obtained by a model without interference.

If a complete model fitting is not desired, either for practical or for speed reasons (in particular when a large amount of data is to be analysed, as in time resolved experiments or SAXS mapping), information on the size of the scattering objects can be obtained by simpler estimates. One of these is the radius of gyration, or Guinier radius, R_g that originates from the Guinier approximation which states that at low q, the intensity scattered by a particle of any shape can be expressed by a Gaussian:

$$I_1(q) \underset{q\to 0}{\equiv} (\rho_p - \rho_m)^2 V_p^2 \exp\left(-\frac{q^2 R_g^2}{3}\right) \tag{13}$$

The width of this Gaussian function can be obtained by a Guinier plot, i.e. by plotting $\log(I)$ vs. q^2 (Fig. 2(b)). The slope of the linear part of the Guinier plot is then equal to $-R_g^2/3$. Although in principle only valid for single particles and for non-interacting particles, it is usually a very good estimate of the size of the precipitates. In size dispersed systems, it has been shown that the q-range in which the Guinier approximation is valid is even extended [15]. This enables its use even above the interference peak, if it is observable, as in Fig. 2(b) where it yields to $R_g = 48.3$ Å. For monodisperse spherical precipitates, $R_g = \sqrt{3/5}R$, but we have previously shown [15] that in the case of a log-normal distribution of spheres with σ close to 0.2, $R_g \approx R$.

To estimate the slope of the linear part of the Guinier plot in a way that is consistent between different samples, it is necessary to define the boundaries of the range in which the fit is performed self-consistently. A way to do this is to perform the fit between constant values of qR_g, e.g. in the range $a/R_g < q < b/R_g$ (typical values: $a = 1$, $b = 2$). As the definition of the fitting range depends on R_g, one has to iterate the process, starting with an estimation of R_g and stopping the iteration when convergence is obtained.

Another instructive representation of the data is the Kratky plot Iq^2 vs. q. Fig. 2(c) is a typical example, where the curve reaches a maximum at q_m before going back to zero. In the spherical case, the position of this maximum is related to R_g through:

$$R_g = \frac{\sqrt{3}}{q_m} \tag{14}$$

This expression can give the first estimate of the Guinier radius necessary to the iterative linear fit. The validity of Eq. (14) was shown to be true on a wide range of dispersion [15]. In the present case, however, Eq. (14) yields to a value of $R_g = 40$ Å. The discrepancy with the value obtained through a Guinier plot ($R_g = 48.3$ Å) can be, in the absence of visual inspection, an indication of the presence of an interference peak in the intensity (i.e. a large volume fraction).

The Kratky plot is also of fundamental importance because it gives a visual hint of the volume fraction of precipitate. It is related to the so-called *invariant* Q, which in the isotropic case writes:

$$Q = \iiint_V I(q_x, q_y, q_z)\,\mathrm{d}q_x\,\mathrm{d}q_y\,\mathrm{d}q_z = \int_0^\infty I(q)q^2\,\mathrm{d}q \tag{15}$$

The reason for the invariance of Q is related to the fact that the total integrated scattered intensity must be proportional to the total excess scattering length density. It is related to the volume fraction f_v by:

$$Q = \int_0^\infty I(q)q^2\,\mathrm{d}q = 2\pi^2(\rho_p - \rho_m)^2 f_v(1 - f_v) \tag{16}$$

Eq. (16) shows that, for small f_v, Q is proportional to f_v, so that the area below the Kratky plot (in red in Fig. 2(c)) is a measure of the precipitate volume fraction. This fact considered together with the position of the maximum of the curve which is inversely proportional to R_g, it is evident that the comparison of two experimental SAS patterns on a Kratky plot is visually extremely rich.

The calculation of Q necessitates integration between 0 and ∞, which is experimentally infeasible. In practice, the small-angle intensity is recorded between a $q_{\min}$ and a $q_{\max}$. To account for this, two approximations are made. Firstly, the q-range between 0 and $q_{\min}$ is approximated by the triangle between the origin, $(q_{\min}, Iq^2_{\min})$ and $(q_{\min}, 0)$. Secondly, in the range above $q_{\max}$, the intensity is assumed to follow the Porod law K_p/q^{-4}. Q is then written:

$$Q = \int_0^{q_{\min}} I(q)q^2\,\mathrm{d}q + \int_{q_{\min}}^{q_{\max}} I(q)q^2\,\mathrm{d}q + \int_{q_{\max}}^{\infty} I(q)q^2\,\mathrm{d}q \approx \frac{I(q_{\min})q^3_{\min}}{2} + \int_{q_{\min}}^{q_{\max}} I(q)q^2\,\mathrm{d}q + \int_{q_{\max}}^{\infty} \frac{K_p}{q^2}\,\mathrm{d}q \tag{17}$$

and finally

$$Q \approx \frac{I(q_{\min})q^3_{\min}}{2} + \int_{q_{\min}}^{q_{\max}} I(q)q^2\,\mathrm{d}q + \frac{K_p}{q_{\max}} \tag{18}$$

where K_p was determined while fitting Eq. (11) for measuring I_{Laue}. K_p can be observed in another possible representation of the data, the Porod plot Iq^4 vs. q (Fig. 2(d)). The horizontal asymptote of the Porod plot is given by K_p. The amplitude of the oscillations of the data around this value decreases when the size dispersion increases. In a monodisperse spherical case, the position of the maximum of the Porod plot is equal to $2.75/R$. In the present case, this yields to a value of 53.7 Å. The discrepancy with the Guinier radius ($R_g = 48.3$ Å) is a consequence of the size dispersion.

In the Porod regime, it is also interesting to consider the Porod radius R_p. It represents the radius of a sphere of surface-to-volume ratio equal to that of the precipitate size distribution. It is given by:

$$R_p = \frac{3V_t}{S_t} \tag{19}$$

where V_t and S_t are the total volume and total surface of the precipitate population in the sample. It is related to the Porod constant K_p through:

$$R_p = \frac{3Q}{\pi K_p} \tag{20}$$

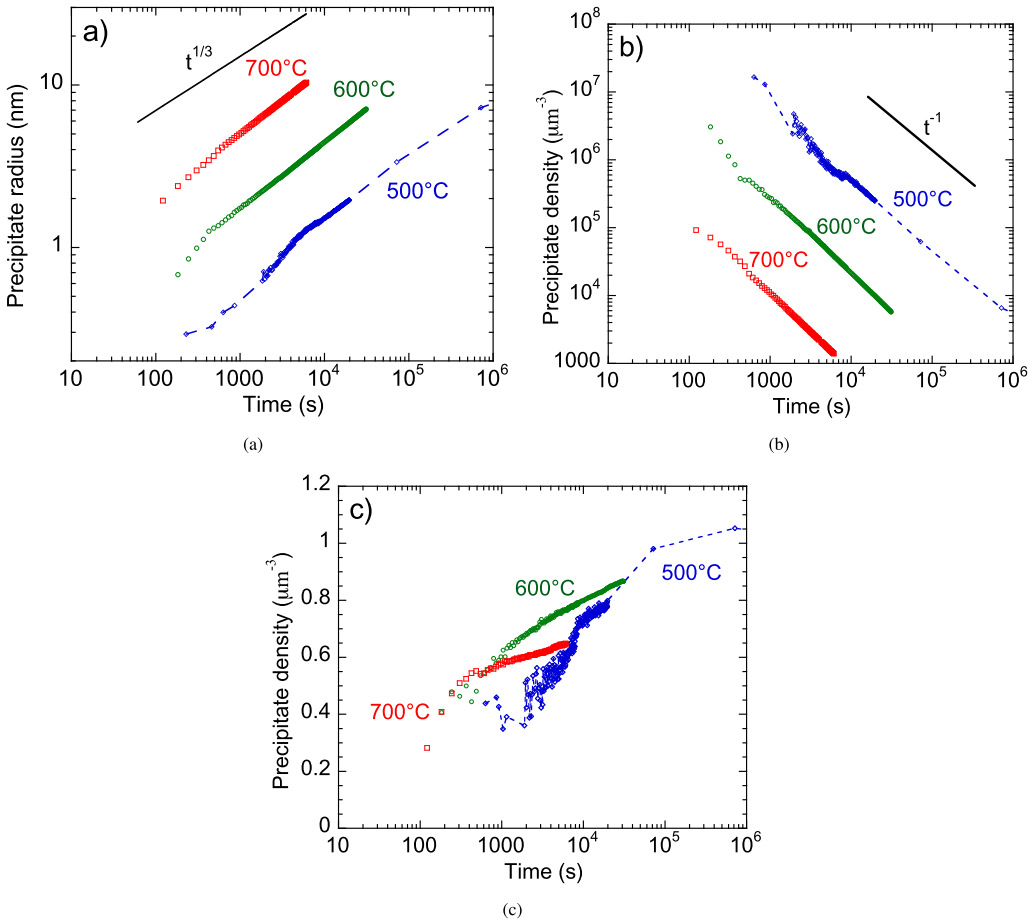

Fig. 3. Example of kinetic measurements realised in-situ on a Fe–Cu alloy at three temperatures: (a) Precipitate radius; (b) precipitate density; (c) precipitate volume fraction.

R_p is equal to the radius in the monodisperse spherical case, whereas for a log-normal size dispersion and σ close to 0.25, it is equal to R_g. Comparisons of the value of R, R_g and R_p for different values of the dispersion can be found in [15].

4. Example of kinetic measurement using SAXS

We will here give a first example of a kinetic measurement, namely for precipitation of Cu in Fe. This system has been thoroughly studied in the literature, both for structural applications (nuclear power plants, Cu-bearing steels), and as a model system. Indeed, it is a binary system, where precipitates are spherical (at least in the first stages of precipitation), the volume fraction relatively low (about 1%), and the precipitates of known composition (almost pure Cu).

In this study, in-situ measurements of the precipitation kinetics were performed by SAXS in an Fe–1.4 wt% Cu binary alloy at three temperatures, namely 500, 600 and 700 °C. The measurement conditions were the following: the X-ray energy was chosen to be 7104 eV, very close to the Fe K-edge so as to improve the scattering contrast between the precipitates and matrix. From these data it was possible to measure accurately the Guinier radius of the precipitates (which is very close to the average precipitate size in the present case), and their volume fraction. Additionally, the precipitate number density can be accessed from the two above data since $N \propto (3f_v)/(4R^3)$ for spherical precipitates.

These data are represented in Fig. 3. The complete precipitation kinetics is obtained. Using this data, it can be observed that the material quickly enters a regime where precipitates coarsen, as the precipitation density decreases with time. It is noteworthy that this regime starts when the volume fraction is significantly different from the equilibrium one. During the coarsening regime, the exponents for the evolution of precipitate size and density are respectively $1/3$ and -1, in precise agreement with the LSW coarsening theory. Such data can be used in order to calibrate a precipitation model; for a more complete account on the use of this data for an estimation of Cu solubility in Fe see [16], and for the use of this data in order to calibrate precipitation models see [17].

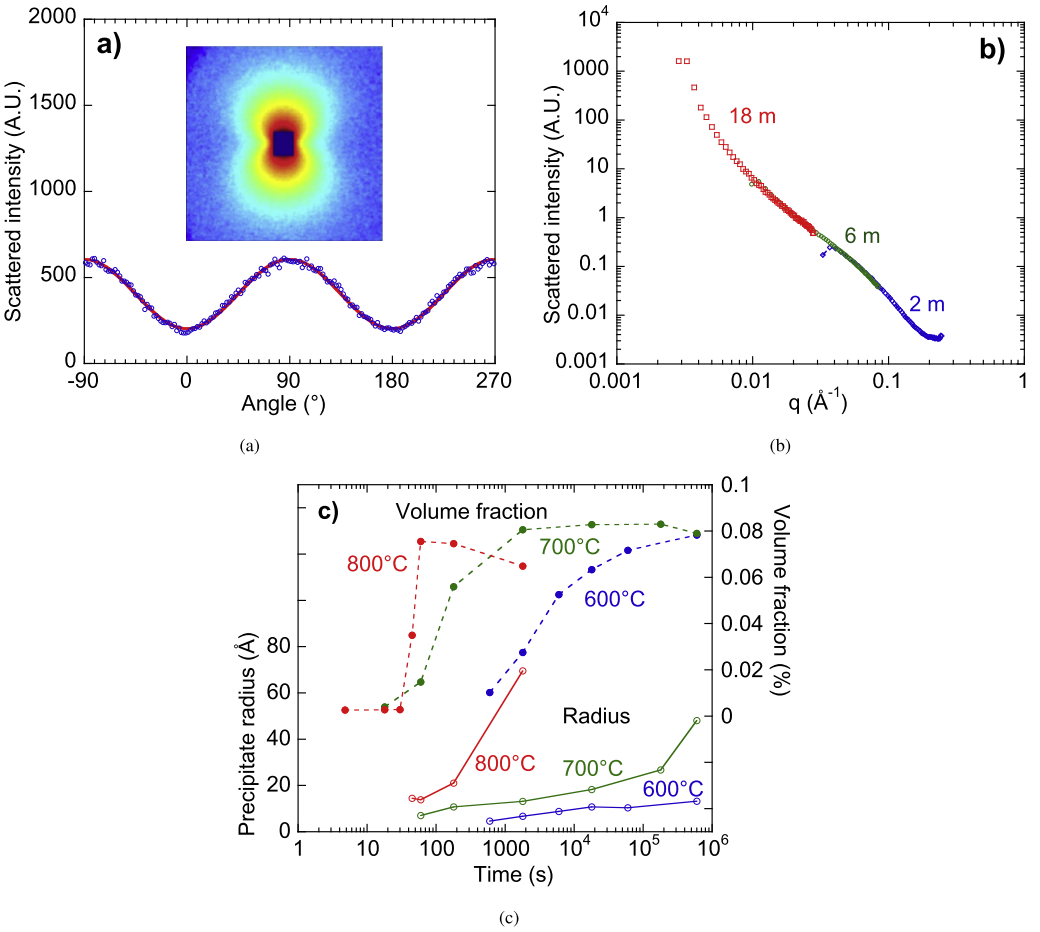

Fig. 4. Example of kinetic measurements realised by SANS on a Fe–Nb–C alloy at three temperatures: (a) Image of the scattered intensity and angular dependence of the intensity at a given vector q due to the combination of nuclear and magnetic contrasts; (b) superposition of measurements made at three sample-to-detector distances in order to increase the q-range dynamics; (c) precipitate size and volume fraction.

5. Example of kinetic measurements using SANS

We will here give a second example of a kinetic measurement by small-angle scattering, this time using neutrons. We study the precipitation of NbC in Fe in the temperature range 500–800 °C, relevant for microalloying applications. Precipitates of NbC appear in low volume fraction (at maximum 0.1%), on the dislocations of ferrite obtained by rapid quenching from austenite. The combination of a highly deformed ferrite (which promotes multiple diffraction), low volume fraction of precipitates and low contrast of electronic density between Fe and NbC make X-ray measurement extremely difficult if not impossible. However, NbC precipitates are non-magnetic, and thus if the Fe matrix is magnetically saturated (which is ensured for a magnetic field of about 1.3 T), a very good magnetic contrast between the precipitates and matrix can be achieved with SANS, making the measurement of very small volume fractions possible (down to 0.01%).

Fig. 4 shows the evaluation of precipitate size (via the Guinier radius) and volume fraction for several ageing temperatures. It is observed for example that the precipitation kinetics is notably faster when the temperature is raised (and therefore that the nose of the TTT diagram for precipitation is at higher temperatures), and that the nucleation radius is only mildly temperature dependent, whereas precipitate growth is extremely sensitive to the ageing temperature. More details on this study can be found in [11,18].

6. Evaluation of precipitate composition in multi-constituent alloys

In multi-constituent alloys, precipitate phases are often non-stoichiometric. Their composition in the different chemical species is not fixed, and can vary with time or temperature of the precipitation heat treatment. When these species have X-ray edge energies in the ranges accessible to X-ray measurements, it is possible to obtain information on the composition contrast between the precipitate and matrix phases. If in addition the matrix has a low concentration of this element, the precipitate composition can be evaluated using X-ray contrast variation, so called the anomalous effect, where SAXS images

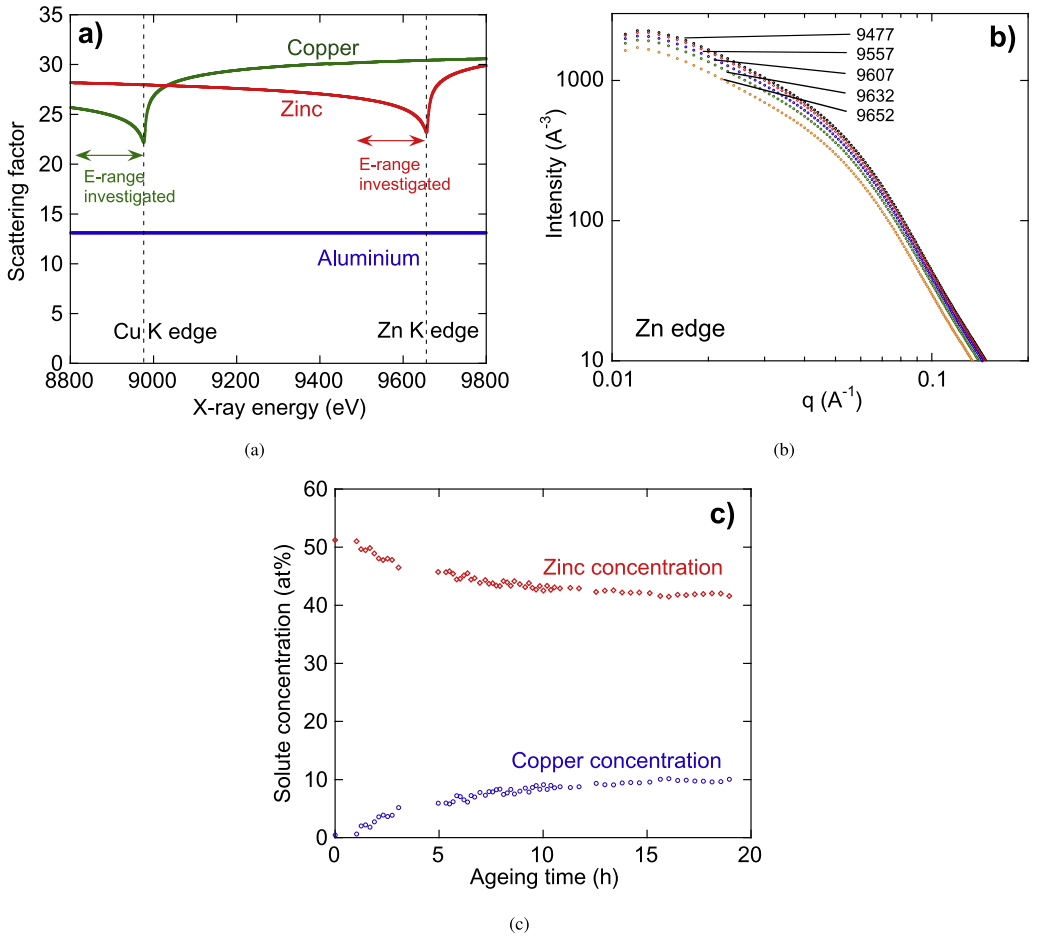

Fig. 5. Example of kinetic measurements realised by ASAXS on an Al–Zn–Mg–Cu alloy. (a) Energy dependence of real scattering factors (f') for Al, Cu and Zn in the energy range investigated, which includes the Cu and Zn K-edges; (b) energy dependence of scattered intensity in the energy range close to the Zn edge; (c) calculated evolution of Zn and Cu concentrations with the precipitates during ageing at 160 °C.

are recorded at several energies close to (and slightly below, in order to avoid fluorescence) the edge of the element of interest. Actually a quantitative estimate of the precipitate composition is not possible without further information on e.g. other species composition, matrix composition or volume fraction. These can be obtained indirectly by other methods such as atom probe tomography. Anomalous SAXS studies are compatible with in-situ measurements with the requirement of high resolution in energy and very low counting times, restricting the measurements to synchrotron sources.

An example is given here of an in-situ ASAXS study of precipitate composition in an Al–Zn–Mg–Cu alloy, AA7150, where precipitates of $Mg(Zn, Al, Cu)_2$ (η phase) form during a heat treatment at 150 °C. This study was concerned with the substitution of Zn with Al and Cu and its evolution with time during the heat treatment. For this purpose the ASAXS measurements were carried out at several energies close to the Zn and Cu K-edges. Close to an absorption edge of an element, its X-ray diffusion factor can be written as:

$$f = f' + \mathrm{i}f'' \tag{21}$$

where f' is the real part of the diffusion factor, that equals the atomic number Z when the energy lies far from the edge energy, and f'' is the imaginary part of the diffusion factor, related to absorption, which varies most at energies above the absorption edge (due to fluorescence). Fig. 5(a) shows the variation of the diffusion factor with X-ray energy at the Cu and Zn edges. These contrast variations result in changes in the measured SAXS intensity, as shown in Fig. 5(b). For this particular case, changing the X-ray energy close to the Zn edge modifies considerably the SAXS intensity. At the Cu edge the SAXS intensity variation is much smaller. Qualitatively one can already say that the precipitates contain a high concentration in Zn and a low concentration in Cu. The detailed quantitative analysis of the data is beyond the scope of this paper and can be found in [19]. It can be applied to an in-situ evaluation of precipitate composition during a 160 °C heat treatment. Fig. 5(c) shows that substitution of some of the Zn by Cu occurs during the heat treatment, related to the slower diffusivity of Cu in Al as compared to that of Zn.

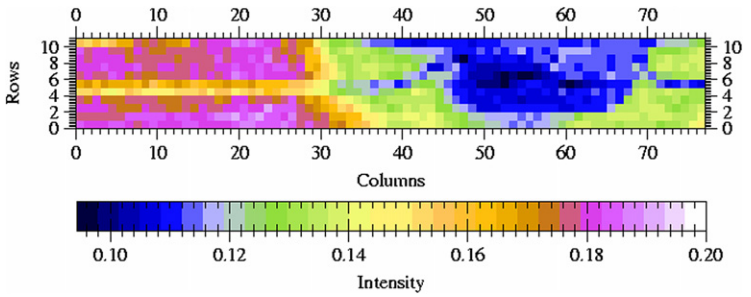

Fig. 6. Map of integrated intensity (proportional to precipitate volume fraction) in the cross-section of a friction stir weld of an AA7475–T76 aluminium alloy. Spacing between data points is 0.5 mm.

7. Application in microstructure mapping

A characteristic of SAS is the possibility to provide a measurement of the size and volume fraction of precipitates from a single scattering image recorded with a 2D detector such as a CCD for X-rays. These measurements can be easily automated, and thus it is possible to proceed with microstructure mapping by scanning the sample with an X-ray beam and recording the scattered image on each point of a grid. With synchrotron sources, measurement times (including data transfer from the CCD and sample displacement) can be of the order of a few seconds, and therefore it is feasible to record microstructure maps of several thousand points. This type of mapping is particularly useful when dealing with heterogeneous materials where the precipitate microstructure is known to be spatially distributed, such as in welds.

Fig. 6 shows an example of such a microstructure map, realised on a friction stir weld of a 7475 (Al–Zn–Mg–Cu) alloy in the T76 initial state (overaged state, containing a high volume fraction of equilibrium η phase). On this map the integrated intensity is represented, which is proportional to the precipitate volume fraction. It appears that the precipitates initially present are totally dissolved in the welded nugget, and that the extent of this dissolution becomes smaller when one gets away from the weld centre. Additional information in this particular case is the presence in the centre of the plate of a zone of smaller volume fraction, which is related to the lower total solute content of the alloy due to macrosegregation. It can be observed that this plate centre-line is displaced by the plastic deformation due to welding towards the top surface of the weld. Finally, the extent of the precipitate dissolution zone is shown to be larger at the top of the plate as compared to the bottom, which reflects the fact that the heat comes essentially from the tool friction in FSW, and therefore from the top surface of the plate. A thorough microstructure mapping study examples can be found in [20,21].

8. Conclusion

We have shown in this article the basic methodology for using small-angle scattering techniques for the quantification of precipitation in metallic systems. Such measurements are relatively easy to perform, however bad hypothesis can easily lead to very wrong interpretations. Obtaining reliable data requires a prior (qualitative) knowledge of precipitate morphology, polydispersity, and if possible chemical composition. For this purpose it is particularly powerful to couple SAS techniques with local techniques. If such precautions are taken, SAS provides unmatched precision for kinetic measurements, especially on size and volume fraction, and the obtained results are reliable inputs for models. Precipitation mapping appears also to be a powerful, even though less widespread in physical metallurgy, application of this technique.

Acknowledgements

Most of the results presented here have been obtained at the ESRF synchrotron source on the D2AM–BM02 beamline, and at the ILL neutron source on the D22 beamline. Scientific and technical support of these beamlines is gratefully acknowledged (J.F. Berar, N. Boudet, B. Caillot, C. Dewhurst). The following colleagues are also acknowledged for their active support with the presented examples: F. Bley, T. Marlaud, M. Perez, F. Perrard, T. Mourey.

References

[1] E. Clouet, L. Laé, T. Epicier, W. Lefebvre, M. Nastar, A. Deschamps, Complex kinetic pathways in multi-component alloys: a multi-scale approach, Nat. Mater. 5 (2006) 482–488.
[2] A. Guinier, G. Fournet, Small-Angle Scattering of X-Rays, John Wiley & Sons, New York, 1955.
[3] A. Guinier, G. Fournet, C.B. Walker, G.H. Vineyard, Small-angle scattering of X-rays, Phys. Today 9 (1956) 38.
[4] O. Glatter, O. Kratky, Small Angle X-Ray Scattering, Academic Press, London, 1982.
[5] G. Kostorz, Small-angle scattering studies of phase separation and defects in inorganic materials, J. Appl. Cryst. 24 (5) (1991) 444–456.
[6] G. Kostorz, X-ray and neutron scattering, Phys. Metall. 4 (1996) 1116–1199.
[7] G. Goerigk, H. Haubold, O. Lyon, J.P. Simon, Anomalous small-angle x-ray scattering in materials science, J. Appl. Cryst. 36 (2003) 425.
[8] O. Glatter, A new method for the evaluation of small-angle scattering data, J. Appl. Cryst. 10 (5) (1977) 415–421.

[9] O. Glatter, Determination of particle-size distribution functions from small-angle scattering data by means of the indirect transformation method, J. Appl. Cryst. 13 (1) (1980) 7–11.
[10] D. Tatchev, R. Kranold, Maximum-entropy method as a routine tool for determination of particle size distributions by small-angle scattering, J. Appl. Cryst. 37 (1) (2004) 32–39.
[11] F. Perrard, A. Deschamps, F. Bley, P. Donnadieu, P. Maugis, A small-angle neutron scattering study of fine-scale NbC precipitation kinetics in the Fe–Nb–C system, J. Appl. Cryst. 39 (4) (2006) 473–482.
[12] A. Deschamps, M. Militzer, W.J. Poole, Precipitation kinetics and strengthening of a Fe–0.8 wt% Cu alloy, ISIJ Int. 41 (2) (2001) 196–205.
[13] M. Dumont, W. Lefebvre, B. Doisneau-Cottignies, A. Deschamps, Characterisation of the composition and volume fraction of [eta]' and [eta] precipitates in an Al–Zn–Mg alloy by a combination of atom probe, small-angle x-ray scattering and transmission electron microscopy, Acta Mater. 53 (10) (2005) 2881–2892.
[14] J. Percus, G. Yevick, Analysis of classical statistical mechanics by means of collective coordinates, Phys. Rev. 110 (1) (1958) 1–13.
[15] A. Deschamps, F. De Geuser, On the validity of simple precipitate size measurements by small-angle scattering in metallic systems, J. Appl. Cryst. 44 (2) (2011) 343–352.
[16] M. Perez, F. Perrard, V. Massardier, X. Kleber, A. Deschamps, H.D. Monestrol, P. Pareige, G. Covarel, Low-temperature solubility of copper in iron: experimental study using thermoelectric power, small angle x-ray scattering and tomographic atom probe, Philos. Mag. 85 (20) (2005) 2197–2210.
[17] A. Deschamps, C. Genevois, M. Nicolas, F. Perrard, F. Bley, Study of precipitation kinetics: towards non-isothermal and coupled phenomena, Philos. Mag. 85 (26) (2005) 3091–3112.
[18] F. Perrard, P. Donnadieu, A. Deschamps, P. Barges, TEM study of NbC heterogeneous precipitation in ferrite, Philos. Mag. 86 (27) (2006) 4271–4284.
[19] T. Marlaud, A. Deschamps, F. Bley, W. Lefebvre, B. Baroux, Influence of alloy composition and heat treatment on precipitate composition in Al–Zn–Mg–Cu alloys, Acta Mater. 58 (1) (2010) 248–260.
[20] C. Genevois, A. Deschamps, A. Denquin, B. Doisneau-Cottignies, Quantitative investigation of precipitation and mechanical behaviour for AA2024 friction stir welds, Acta Mater. 53 (8) (2005) 2447–2458.
[21] M. Dumont, A. Steuwer, A. Deschamps, M. Peel, P.J. Withers, Microstructure mapping in friction stir welds of 7449 aluminium alloy using SAXS, Acta Mater. 54 (2006) 4793–4801.